materials

MDPI

Article

Temperature-Dependent Creep and Mesoscopic Mechanisms of Basalt Fiber-Reinforced Asphalt Concrete: Experiments and Discrete Element Simulations

Kaituo Wang [1,2], Shuochang Xu [1,2,*], Ruize Han [2], Dinghan Fang [1,3,†], Yintao Wang [2] and Yan Liu [4]

[1] School of Civil Engineering and Water Conservancy, Qinghai University, Xining 810016, China; wangkaituo_917@163.com (K.W.)
[2] School of Civil and Transportation Engineering, Qinghai Minzu University, Xining 810007, China
[3] College of Water Conservancy and Hydropower Engineering, Hohai University, Nanjing 210098, China
[4] School of Engineering, Qinghai Institute of Technology, Xining 810016, China
* Correspondence: xuscqinql@163.com
† Current address: College of Water Conservancy and Hydropower Engineering, Hohai University, Nanjing 210098, China.

Abstract

Basalt fiber-reinforced asphalt concrete (BFAC) is used in hydraulic anti-seepage structures, where sustained loading and temperature variations can compromise deformation control. This study combines triaxial creep tests with discrete element simulations to examine the effects of basalt fiber (BF), temperature, confining pressure, fiber length, and fiber content on creep and contact-scale load transfer. Under −4 °C, 0.4 MPa confining pressure and 1.5 MPa axial stress, addition of BF reduced the average creep rate from 3.55 × 10^{-6} s^{-1} to 3.21 × 10^{-6} s^{-1}, a descriptive reduction of 9.58%, and increased the number of modeled contact force chains from 12,398 to 15,838 (27.75%). Increasing the confining pressure suppressed creep deformation and produced a denser modeled contact network; at 8 °C, the contact count increased from 7207 to 12,110 (68.0%) as the confining pressure increased from 0 to 0.6 MPa. In the numerical model, higher temperatures increased creep deformation through temperature-dependent viscoelastic softening of asphalt mastic; the strengths of the mastic-aggregate and mastic-fiber parallel bonds did not vary with temperature. Parametric simulations suggest that longer fibers and higher contents delayed the attainment of a common strain threshold; however, the curves crossed and no configuration had the lowest strain at every time. The 9 mm, 0.4% configuration should therefore be considered as the most favorable of the numerically investigated configurations rather than a universally optimal mixture. Only the 9 mm, 0.4% configuration was examined physically. The findings support comparative analysis of hydraulic anti-seepage materials, but long-term extrapolation requires longer experiments and three-dimensional model validation.

Keywords: hydraulic anti-seepage structures; Burgers contact model; confining pressure; viscoelastic parameter calibration; particle load transfer

Academic Editor: Giovanni Polacco

Received: 11 October 2026
Revised: 14 November 2026
Accepted: 20 November 2026
Published: 24 November 2026

Copyright: © 2026 by the authors. Licensee MDPI, Basel, Switzerland. This article is an open access article distributed under the terms and conditions of the Creative Commons Attribution (CC BY) license.

1. Introduction

With the continuous advancement of water resource development and utilization, the number of hydraulic structures such as earth-rock dams, water conveyance canals and

dike projects has been steadily growing. The durability and stability of their anti-seepage structures are important for their safe operation [1–3]. Due to its excellent anti-seepage performance and capacity for deformation coordination, asphalt concrete has been widely applied in the anti-seepage structures of core dams, face slab dams and other hydraulic facilities [4]. However, it is sensitive to environmental changes and exhibits obvious time-dependent deformation behaviors. When used as the anti-seepage material for hydraulic structures, asphalt concrete is prone to creep deformation under the combined action of load and ambient temperature, which may induce structural deformation, material cracking and other engineering defects, seriously endangering the durability, safety and stability of hydraulic structures [5,6]. Therefore, systematic research on the creep deformation behavior of asphalt concrete under the coupled influence of temperature and confining pressure is essential to ensure the seepage resistance and reliable operation of hydraulic engineering projects [7].

Previous studies have modified asphalt concrete using high-strength, high-temperature-resistant and corrosion-resistant basalt fiber (BF) to further improve its mechanical properties and structural stability [8,9]. Long et al. [10] explored how BF improved the mechanical properties of asphalt concrete through uniaxial compression and tensile tests, combined with nanoindentation, scanning electron microscopy (SEM), computed tomography (CT) scanning and other microscopic testing methods. They found that the incorporation of BF improved the compressive strength, tensile strength and other mechanical indicators of asphalt concrete. Zhang et al. [11] adopted pre-cracked three-point bending tests to analyze the effects of asphalt–aggregate ratio and fiber content on the fracture performance of asphalt concrete. Gui et al. [12] studied the effect of modification with BF on the crack resistance of warm-mixed recycled asphalt mixtures via edge-notched disk bending (ENDB), acoustic emission (AE), and SEM tests, and verified that BF could effectively enhance the fracture resistance of materials under freeze–thaw cycles. Hassanjani et al. [13] incorporated short-cut BF into recycled asphalt concrete and conducted semi-circular bending (SCB) tests to investigate its effect on fractures under diverse fracture modes and temperature conditions. The results confirmed that BF could help improve the crack resistance, fracture energy and deformation energy consumption capacity of asphalt materials. Collectively, the above studies have proven that BF can effectively enhance the strength and crack resistance of asphalt concrete. However, in actual service conditions in hydraulic structures, basalt fiber-reinforced asphalt concrete (BFAC) is usually subjected to creep deformation under biaxial or triaxial compression [14]. At the same time, restricted by the temperature sensitivity of asphalt materials, temperature plays a decisive regulatory role in the strength and deformation characteristics of BFAC [15,16]; however, research on this topic remains insufficient. Therefore, it is important to study creep in BFAC under the influence of temperature and confining pressure in order to improve the seepage control of hydraulic structures and analyze their long-term deformation.

Laboratory triaxial creep tests provide effective macroscopic measurements but cannot directly resolve the contact-scale mechanisms of time-dependent deformation [17,18]. The discrete element method (DEM) has therefore been used to investigate particle motion and mesoscopic load transfer in heterogeneous asphalt materials [19–21]. Wang et al. [22] used a three-dimensional Particle Flow Code (PFC) model and thermal-expansion-based thermo-mechanical coupling to study creep damage at 34, 42, and 50 °C. Wang et al. [23], Zhang et al. [24], and Ma et al. [25] incorporated Burgers or related viscoelastic representations, but their material parameters were calibrated for discrete thermal conditions or their studies addressed different structural effects. These approaches do not provide a continuous relationship between temperature and Burgers contact parameters for BFAC over the range examined here. The methodological contribution of this study is the con-

tinuous adjustment of mastic Burgers parameters with temperature and their implementation through macro–meso conversion, not a new thermal expansion coupling scheme or a new fiber representation method. This approach allows temperature-dependent mastic softening to be updated at the contact level while keeping interface bond parameters explicitly separate.

Accordingly, this study combines laboratory triaxial creep tests with DEM simulations to examine BFAC under temperatures of −4, 0, 4, and 8 °C and confining pressures of 0, 0.2, 0.4, and 0.6 MPa. The specific objectives are to (1) establish continuous temperature-dependent relationships for the Burgers parameters and implement them in mastic-mastic contacts through macro–meso parameter conversion; (2) quantify the creep response under different thermal and confinement conditions and interpret the associated change in force chain and particle displacement; and (3) use the calibrated model to compare fiber lengths and contents that were not varied in the physical tests. The contribution is therefore a parameterized contact-level representation of mastic viscoelastic softening within the investigated temperature range.

2. Materials and Methods

2.1. Experimental Materials

We used grade A Karamay No. 90 asphalt produced by PetroChina Karamay Petrochemical Company, Karamay City, China. Its main technical indicators were measured in accordance with DL/T 5362—2018 [26], *Test Code for Hydraulic Asphalt Concrete*, and are listed in Table 1.

Table 1. Technical indicators of Karamay No. 90 asphalt.

Indicator	Result	Technical Requirements
Penetration (0.1 mm)	88.52	80–100
Ductility (cm)	23.23	≥20
Softening Point (°C)	47.51	≥44
Density (g/cm^3)	1.02	Measured value

Both coarse and fine aggregates were produced by crushing basalt, and basalt mineral powder was used as filler. The physical and mechanical properties of the aggregates were measured in accordance with DL/T 5362—2018 [26] and are presented in Table 2.

Table 2. Physical and mechanical properties of the aggregates.

Indicator	Result	Technical Requirements
Oversize particle ratio (%)	1.44	≤5
Apparent density (g/cm^3)	2.81	≥2.6
Adhesion with asphalt (Grade)	5	≥4

The optimal asphalt–aggregate ratio was determined to be 6.9% by laboratory Marshall tests, and mineral powder accounted for 12% of the total mineral aggregate mass. According to Hui et al. [27], suitable BF lengths and contents are 6–9 mm and 0.2–0.4% of the total asphalt–concrete mass, respectively. A fiber length of 9 mm and a content of 0.4% were selected within these reported ranges and held constant in all physical BFAC tests; this selection was not assumed to be optimal a priori. The BF was purchased from Zhengzhou Dengdian Basalt Fiber Co., Ltd. (Zhengzhou, Henan Province, China), and the technical properties listed in Table 3 were provided by the manufacturer.

Table 3. Performance indicators of BF.

Indicator	Result
Elastic Modulus (GPa)	92
Density (g/cm^3)	2.63
Monofilament Diameter (μm)	10
Thermal Conductivity (W/(m·K))	0.03

The gradation curve of the aggregates used in the asphalt concrete is shown in Figure 1. The aggregate fractions were weighed separately according to this gradation, with mineral powder accounting for 12% of the total mineral aggregate mass. The mass ratio of asphalt to the total mineral aggregates was 6.9%. The BF length was 9 mm, and the BF content was 0.4% of the asphalt mixture's total mass.

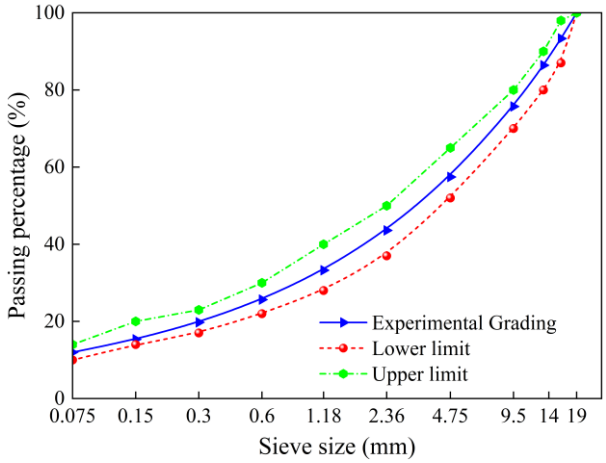


Figure 1. Gradation curve of asphalt concrete.

For specimen preparation, the mineral aggregates were first dried in an oven at (105 ± 5) °C for 4–6 h until a constant mass was reached. After being weighed according to the specified gradation, they were preheated to 180 °C, while the asphalt was heated to 150 °C. The preheated mineral aggregates and the weighed BF were then transferred to an asphalt mixture mixer preheated to 165 °C and dry-mixed for 60 s to disperse the fibers uniformly throughout the mineral aggregates. The asphalt was subsequently added, and mixing continued for another 60 s until the surfaces of the mineral aggregates were uniformly coated with asphalt. The mixture was placed in rectangular molds and compacted on a compaction platform. After cooling to room temperature and demolding, cylindrical specimens with a diameter of 100 mm and a height of 100 mm were obtained by coring for subsequent creep tests.

2.2. Experimental Methods and Scheme

The creep deformation of asphalt concrete can be generally divided into three stages: instantaneous deformation, steady-state creep, and accelerated creep. Affected by microcrack propagation and local damage, the internal stress state of materials in the accelerated creep stage is complex, and the strain development shows obvious nonlinearity and discreteness, which fails to reflect the intrinsic creep characteristics of asphalt concrete [28,29]. Therefore, this stage is usually excluded from the main analysis of material creep performance in engineering research [30].

To investigate the creep properties of BFAC, cylindrical specimens with dimensions of Φ100 mm × 100 mm were fabricated. Considering the service conditions of hydraulic anti-seepage structures and the ambient temperatures of Northwest China [31], triaxial creep tests were performed under four confining pressures (0, 0.2, 0.4, and 0.6 MPa) and four temperatures (−4, 0, 4, and 8 °C). Three parallel specimens were tested for each material group and temperature-confining-pressure combination, and the arithmetic mean curves were used for analysis. Before loading, each specimen was conditioned at the target temperature until thermal equilibrium was reached, and the target temperature was maintained throughout testing. Temperature conditioning and loading were performed in accordance with DL/T 5362—2018 [26]. The prescribed confining pressure was applied and held constant, after which the axial stress was increased to the selected value of 1.5 MPa and maintained for the creep measurement. A schematic of the test equipment and photographs of the specimen and testing process are shown in Figure 2a,b, respectively.

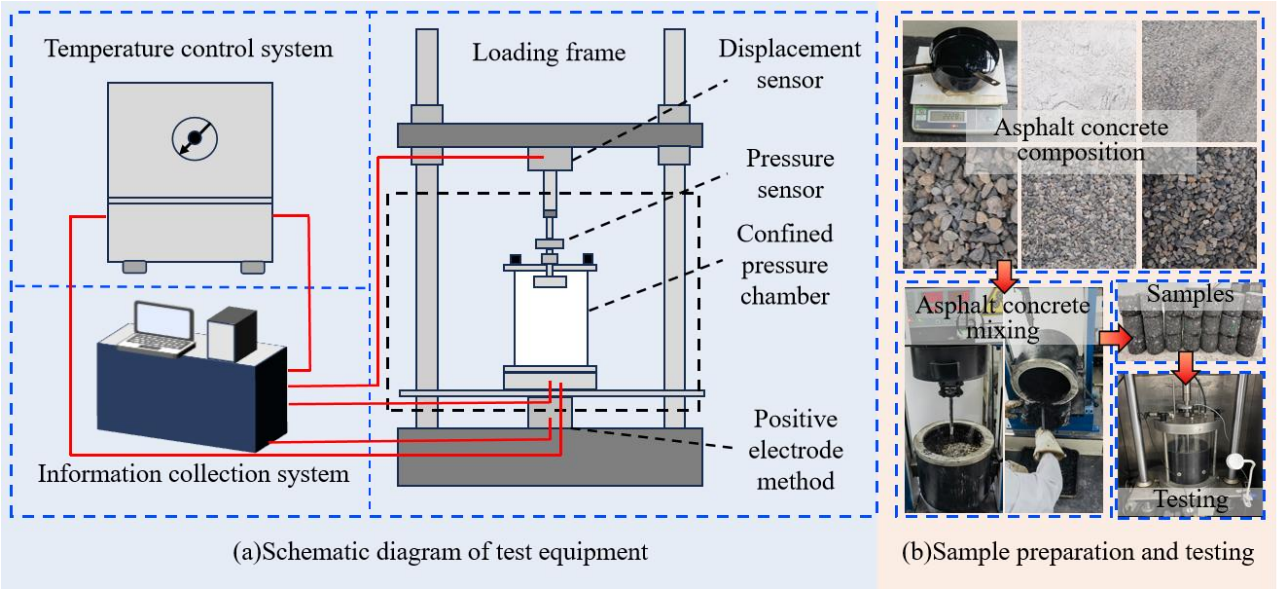


Figure 2. BFAC creep test equipment and testing.

Before the creep tests, triaxial compression tests were conducted at 25 °C and 0 MPa confining pressure, as shown in Figure 3. Following Wen et al. [32] and Tarifard et al. [33], 35% of the resulting ultimate compressive strength, namely 1.5 MPa, was selected as a common reference axial stress for all creep conditions. Using the same axial stress enables temperature and confining-pressure effects to be compared without simultaneously changing the applied load; it does not imply a constant stress-to-strength ratio at every temperature. This limitation is relevant because temperature-dependent strength may alter the relative loading level. Each laboratory creep test was terminated after 8 h or when axial strain reached 10%, whichever occurred first; this termination rule did not constrain the numerical simulations.

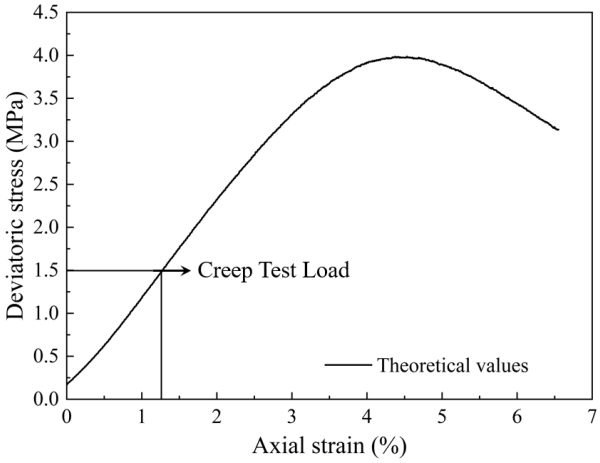


Figure 3. Triaxial compression test result.

3. Constitutive Model

3.1. Burgers Model Parameter Adjustment Method Considering the Influence of Temperature

Burgers elements were introduced in the normal and tangential contact directions to represent the viscoelastic behavior of particle contacts under compression. The corresponding macroscopic Burgers constitutive model is given in Equation (1).

$$\varepsilon(t) = \frac{\sigma}{E_1} + \frac{\sigma}{E_2} + \frac{\sigma}{\eta_1} t - \frac{\sigma}{E_2} e^{-\frac{E_2}{\eta_2} t} \quad (1)$$

In Equation (1), ε is the axial strain (dimensionless), σ is the axial stress (MPa), t is the creep time (s), E_1 and E_2 are the Maxwell and Kelvin elastic moduli (MPa), respectively, and η_1 and η_2 are the corresponding Maxwell and Kelvin viscosity coefficients (MPa·s).

Uniaxial creep curves of asphalt mastic specimens were obtained through uniaxial creep tests. Subsequently, fitting with Equation (1) yielded the four macroscopic creep parameters of the Burgers model at varying temperatures, as listed in Table 4.

Table 4. Burgers model parameters at varying temperatures.

Temperature (°C)	E_1 (MPa)	E_2 (MPa)	η_1 (MPa·s)	η_2 (MPa·s)
−4	1236.9	540.4	64,481.3	16,821.2
0	1011.4	370.2	5371.4	4113.9
4	950.4	292.4	4153.1	3327.2
8	880.2	215.6	3150.8	2538.1

Asphalt exhibits distinct temperature sensitivity. The temperature coupling module in the PFC mainly adopts the particle expansion method, that is, by introducing the thermal expansion coefficient, the temperature change is transformed into the particle size adjustment, which causes the adjustment of the internal contact state of the particles and the corresponding mechanical response. This method has good applicability in rock materials and the study of freeze–thaw problems [34,35]. However, the temperature-induced softening effect of asphalt concrete mainly stems from the change in material properties, while the contribution of particle geometric thermal expansion is limited [36]. Consequently, the thermal expansion coupling method cannot accurately describe the temperature sensitivity of asphalt concrete in PFC.

To represent temperature sensitivity without prescribing particle thermal expansion, the Burgers contact parameters were updated as functions of temperature T. Equations

(2)–(5) were calibrated using the four measured temperatures (−4, 0, 4, and 8 °C). A piecewise strategy at 0 °C was adopted because a single expression did not reproduce all four measured points with satisfactory accuracy. For 0 °C ≤ T ≤ 8 °C, E_1, E_2, and η_2 were fitted by linear least squares, whereas η_1 was fitted by an exponential least-squares expression. For −4 °C ≤ T < 0 °C, exponential branches anchored at the measured 0 °C values were calibrated to pass through the corresponding −4 °C measurements. The 0–8 °C branches must not be extrapolated to −4 °C.

Back-substitution at the four calibration temperatures gave maximum absolute relative deviations of 0.39%, 0.14%, 0.66%, and 0.03% for E_1, E_2, η_1, and η_2, respectively, between the printed expressions and Table 4; these deviations reflect both the fitting residuals at the calibration points and rounding of the fitted coefficients in the printed expressions.

$$E_1(T)=\begin{cases}1011.4\mathrm{e}^{-0.050318T} & -4\le T<0\\ 1011.4-16.170T & 0\le T\le 8\end{cases} \tag{2}$$

$$E_2(T)=\begin{cases}370.2\mathrm{e}^{-0.094567T} & -4\le T<0\\ 370.2-19.35T & 0\le T\le 8\end{cases} \tag{3}$$

$$\eta_1(T)=\begin{cases}5371.4e^{-0.621322T} & -4\le T<0\\ 5371.4e^{-0.06597T} & 0\le T\le 8\end{cases} \tag{4}$$

$$\eta_2(T)=\begin{cases}4113.9e^{-0.352067T} & -4\le T<0\\ 4113.9-196.917T & 0\le T\le 8\end{cases} \tag{5}$$

In Equations (2)–(5), T is temperature (°C); E_1 and E_2 are expressed in MPa, and η_1 and η_2 are expressed in MPa·s. The first branch applies for −4 °C ≤ T < 0 °C, and the second branch applies for 0 °C ≤ T ≤ 8 °C.

For the Burgers model in PFC, mesoscopic contact parameters were obtained from the macroscopic parameters using the conversion relationships reported in the literature and given in Equation (6) [37].

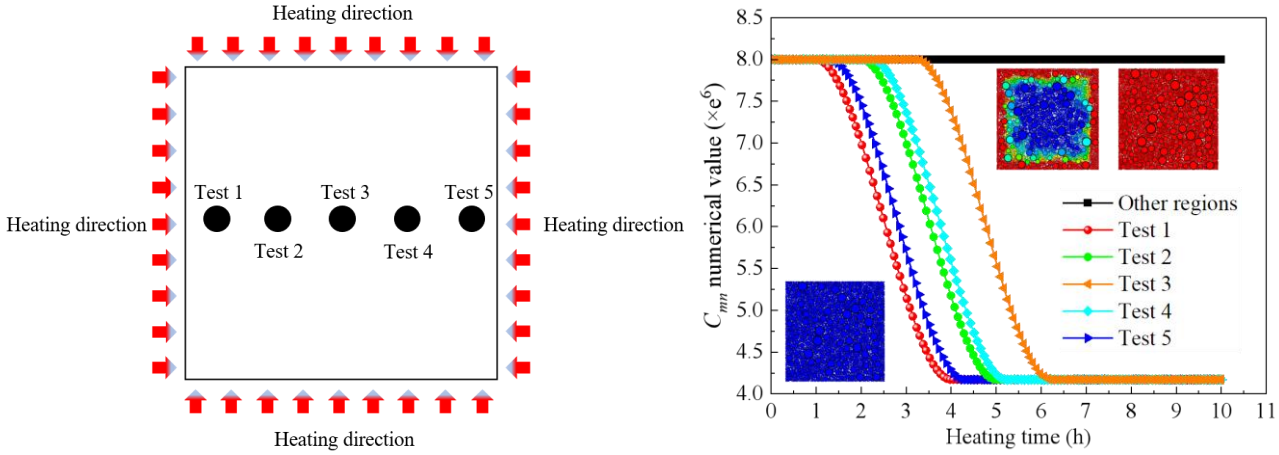
$$\begin{cases}K_{kn}=E_2(T)L\\ C_{kn}=\eta_2(T)L\\ C_{mn}=\eta_1(T)L\\ K_{mn}=E_1(T)L\\ K_{ks}=\dfrac{E_2(T)L}{2(1+v)}\\ C_{ks}=\dfrac{\eta_2(T)L}{2(1+v)}\\ K_{ms}=\dfrac{E_1(T)L}{2(1+v)}\\ C_{ms}=\dfrac{\eta_1(T)L}{2(1+v)}\end{cases} \tag{6}$$

In Equation (6), K_{kn} and C_{kn} are the normal elastic stiffness (MPa·mm) and normal viscosity coefficient (MPa·mm·s), respectively, of the Kelvin element; C_{mn} and K_{mn} are the normal viscosity coefficient (MPa·mm·s) and normal elastic stiffness (MPa·mm), respectively, of the Maxwell element; K_{ks} and C_{ks} are the shear elastic stiffness (MPa·mm) and shear viscosity coefficient (MPa·mm·s), respectively, of the Kelvin element; K_{ms} and C_{ms} are

the shear elastic stiffness (MPa·mm) and shear viscosity coefficient (MPa·mm·s), respectively, of the Maxwell element; ν is the Poisson's ratio of asphalt mastic (dimensionless); and L is the effective contact length (mm).

3.2. Method Validation

To verify the feasibility of the numerical implementation of the model in PFC, a rectangular calculation domain was first established. Then, test units composed of two contacting balls were generated in five monitoring regions, which were assigned the Burgers model, and the corresponding unit IDs were recorded. Subsequently, remaining particles were generated in the calculation domain to achieve model equilibrium, and heat transfer parameters as well as initial temperature were assigned to all particles. The boundary wall temperature was set higher than the initial temperature of the internal balls to drive heat transfer from the boundaries to the interior of the model. During the heating process, the real-time variation in C_{mn} in each test region with heating time was recorded using appropriate monitoring functions. The validation schematic is shown in Figure 4a, and the numerical test results of C_{mn} are presented in Figure 4b.



(**a**) Validation schematic. (**b**) Numerical test results of C_{mn}.

Figure 4. Verification of temperature-dependent Burgers parameter updating.

As heating progressed, C_{mn} decreased in each monitoring region, confirming that the code updated Burgers contact parameters as intended. Figure 4 verifies only the numerical implementation of temperature-dependent parameter updating; it does not establish the predictive accuracy of the complete BFAC model, which is examined separately using the laboratory creep curves in Section 5.2.

3.3. Parallel Bond Model

The mechanical behavior of the parallel bond model comprises two components: linear elastic contact and bonded interface. The point contact behavior was simulated using linear elastic contact, which transmits normal and tangential forces but cannot transfer moments, and is mainly used to characterize loading boundaries and inter-particle contact behaviors [38]. Parallel bond contacts can transmit both forces and moments simultaneously, thereby effectively simulating the bonding and bending resistance between particles. Accordingly, this model is suitable for describing the mechanical characteristics of interfaces between asphalt mastic and aggregates, as well as interfaces between asphalt mastic and BF [39].

4. Discrete Element Modeling of BFAC

4.1. DEM Specimen Generation

In accordance with the particle gradation rules of physical tests, hundreds of thousands to several million balls would be generated in PFC when simulating fine materials such as asphalt and fillers, whose particle sizes are much smaller than those of aggregates. This seriously reduces computational efficiency and imposes high demands on computer performance. To ensure reasonable mechanical responses, reduce the numerical calculation scale, and balance computational accuracy and efficiency, the weighted average method was employed to scale the original gradation system and achieve equivalent grouping of particles, referring to the research by Xue et al. [40] and Zhang et al. [41].

A two-dimensional axial section was adopted to reduce computational cost while retaining gradation, contact evolution, and force-chain rearrangement in the axial-radial plane [37,40]. The axisymmetric triaxial test configuration provides a rationale for comparing conditions under a common two-dimensional idealization [40–42]. Nevertheless, circular disks have different coordination numbers from three-dimensional spheres and omit out-of-plane interlocking; planar wall confinement cannot reproduce the full circumferential constraint of a cylindrical specimen; fibers are restricted to in-plane orientations; and spatial load-transfer networks are reduced to planar force chains. Accordingly, absolute contact counts, crack counts, and displacement fields are model-specific, and the simulations are used primarily for relative comparisons under identical discretization assumptions.

In the PFC modeling process, the asphalt mastic composed of asphalt and fillers was characterized by ball elements with a diameter of 1 mm, while fine and coarse aggregates were characterized by ball elements with diameters ranging 2.36–9 mm [14]. The particle content and equivalent gradation distribution are detailed in Table 5.

Table 5. Content of each particle size fraction in the 2D specimen.

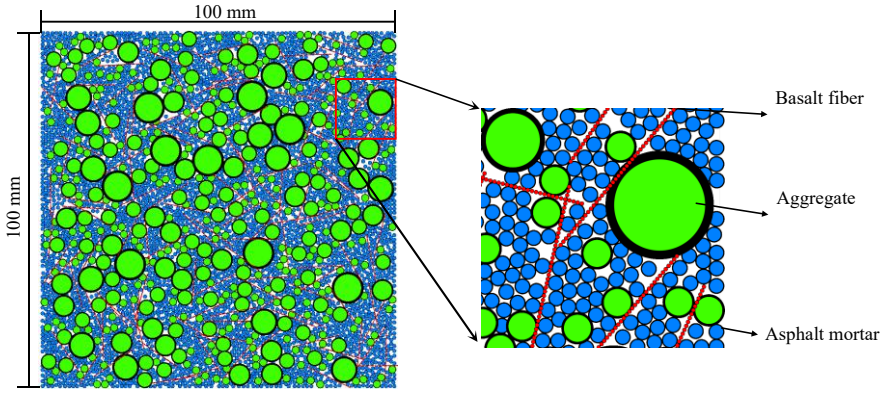
Particle Size Range (mm)	Content (%)
1	43.59
1–2.36	13.86
2.36–4.5	18.27
4.5–6.25	10.64
6.25–7.58	6.93
7.58–9	6.71

BF was represented by equivalent fiber bundles rather than by explicitly modeling individual monofilaments [42]. Each bundle consisted of 45 bonded balls with a radius of 0.1 mm connected in series, giving a nominal diameter of 0.2 mm and a length of 9 mm. For a monofilament diameter of 10 μm, cross-sectional-area equivalence gives $N_f = (0.2/0.01)^2 = 400$ filaments per bundle.

The equivalent axial stiffness satisfies $E_bA_b = N_fE_fA_f$. For the two-dimensional model, the physical fiber mass content was converted using a mass-scaling assumption rather than by directly assigning the fiber mass of the full physical specimen. Specifically, the target fiber mass fraction w, defined relative to the total specimen mass, was applied to the total mass M_{2D} of the two-dimensional modeled specimen, giving $m_f = wM_{2D}$. Under this convention, no separate effective thickness is required because the model thickness and particle-mass scaling are already incorporated in M_{2D}. The number of equivalent bundles was then calculated as $N_b = m_f/(N_f\rho_fA_fl_f)$, where A_f and A_b are the filament and bundle cross-sectional areas, E_f and E_b are their elastic moduli, ρ_f is the filament density, and l_f is the filament length. Using $N_f = 400$, a monofilament diameter of 10 μm, and $\rho_f = 2.63$ g/cm^3,

the equivalent masses of one 3, 6, and 9 mm bundle are 2.479×10^{-4}, 4.957×10^{-4}, and 7.436×10^{-4} g, respectively. The bundle count for each investigated fiber content is obtained by substituting its corresponding w into the above equation. For the 3, 6, and 9 mm fiber lengths, the same tangential ball convention gives 15, 30, and 45 balls per bundle, respectively. Bundles were randomly distributed with in-plane orientations, and the same modeling convention was used for all fiber contents.

Figure 5 shows the full two-dimensional specimen and a local fiber-bundle representation, in which green particles represent aggregates, blue particles represent asphalt mortar, and red chains represent basalt-fiber bundles.



(**a**) Full specimen (**b**) Local fiber-bundle representation

Figure 5. Two-dimensional DEM model of BFAC.

4.2. Constitutive Model Selection and Parameter Calibration

In addition to the intra-bundle BF-BF connections described in Section 4.1, five contact types were defined in the BFAC model: contacts within the asphalt mastic, contacts between the asphalt mastic and aggregates, contacts within aggregates, aggregate-BF contacts, and asphalt mastic-BF contacts. Based on previous studies of PFC contact constitutive models and the material composition of asphalt concrete, the Burgers, parallel-bond, and linear models were assigned to these contacts according to their mechanical functions [40,43,44]. The Burgers model was used for contacts within the asphalt mastic to represent its temperature-sensitive viscoelastic behavior, which plays an important role in the creep deformation of the mixture. Temperature effects were therefore introduced exclusively by adjusting the Burgers parameters of these contacts. The parallel-bond model was used at asphalt mastic-aggregate and asphalt mastic-BF interfaces to describe interfacial adhesion and load transfer. The corresponding parallel-bond parameters were held constant at all temperatures; thus, no temperature-dependent degradation of interfacial stiffness or strength was prescribed. The linear model was used for contacts within aggregates and between aggregates and BF. It also represents the unbonded limiting condition of the parallel-bond model after bond failure [44]. The constitutive models assigned to the different contact types are summarized in Table 6.

Table 6. Contact constitutive models assigned in the BFAC discrete element model.

Contact Type	Contact Model
Internal contact within asphalt mastic	Burgers model
Contacts between asphalt mastic and aggregates; contacts between asphalt mastic and BF	Parallel bond model
Internal contact within aggregate	Linear model
Contact between aggregates and BF	Linear model

The mesoscopic Burgers parameters at different temperatures were obtained from the macroscopic parameters in Table 4 using Equations (2)–(6), with Poisson's ratio set to 0.35. The effective contact length was taken as 1 mm, corresponding to the sum of the radii of two contacting mastic balls with diameters of 1 mm. The normal stiffness and viscosity parameters were determined from the corresponding macroscopic parameters, while the shear parameters were calculated using the adopted Poisson's ratio. These conversions were applied only to contacts within the asphalt mastic; aggregate and interface contacts were described using separately calibrated linear or parallel-bond models. The resulting mesoscopic parameters are listed in Table 7.

Table 7. Mesoscopic parameters of the Burgers model at varying temperatures.

Parameter		Temperature (°C)			
		−4	**0**	**4**	**8**
Kelvin section	K_{kn} (MPa·mm)	540.4	370.2	292.4	215.6
	C_{kn} (MPa·mm·s)	16,821.2	4113.9	3327.2	2538.1
	K_{ks} (MPa·mm)	200.1	137.1	108.3	79.9
	C_{ks} (MPa·mm·s)	6230.1	1523.7	1232.3	940.0
Maxwell section	K_{mn} (MPa·mm)	1236.9	1011.4	950.4	880.2
	C_{mn} (MPa·mm·s)	64,481.3	5371.4	4153.1	3150.8
	K_{ms} (MPa·mm)	458.1	374.6	352.0	326.0
	C_{ms} (MPa·mm·s)	23,882.0	1989.4	1538.2	1167.0

The bonding performance of the parallel bond model in PFC is mainly governed by parameters including parallel bond elastic modulus (pb_emod), tensile strength (pb_ten), cohesion (pb_coh), and internal friction angle (pb_fa). After multiple rounds of parameter calibration, the parallel bond model parameters were determined as shown in Table 8.

Table 8. Parameters of the parallel bond model.

Parameter Name	Value
pb_emod (MPa)	33.2
pb_ten (MPa)	2.6
pb_coh (MPa)	1.3
pb_fa (°)	50

5. Results and Analysis

5.1. Effect of BF on the Creep Characteristics of Asphalt Concrete

To investigate the influence of BF on creep performance, laboratory creep tests were conducted on ordinary asphalt concrete and BFAC specimens (9 mm fiber length and 0.4% fiber content) at −4 °C, a confining pressure of 0.4 MPa, and an axial stress of 1.5 MPa. Three replicate specimens were tested for each material group, and the average creep curves are presented in Figure 6. The inset photographs show the test arrangement and specimens, the adjacent DEM insets show the corresponding numerical representations, and the red arrows link these insets to the two material groups. The curves compare the experimental creep responses of the two mixtures under the stated condition; they are not presented as model validation curves.

As shown in Figure 6, both mixtures exhibited rapid initial strain accumulation followed by a progressive decrease in the slope of the strain-time curve, and no accelerated-creep stage was observed within the 8 h test. Throughout the test, the mean BFAC curve remained below that of ordinary asphalt concrete, indicating lower cumulative axial strain at corresponding loading times, although the two curves remained relatively close. The

average creep rates calculated over the test interval were 3.55×10^{-6} s^{-1} and 3.21×10^{-6} s^{-1} for ordinary asphalt concrete and BFAC, respectively; BF addition therefore reduced the mean creep rate by 9.58%. These results indicate that the 9 mm, 0.4% BF configuration moderately improved creep resistance under the present temperature and stress conditions without changing the overall creep pattern. However, given the specimen-level variability represented by the SD bands and the absence of inferential statistical analysis, this reduction is interpreted as a descriptive difference between the mean curves rather than demonstrated statistical superiority or evidence of a general optimum fiber configuration.

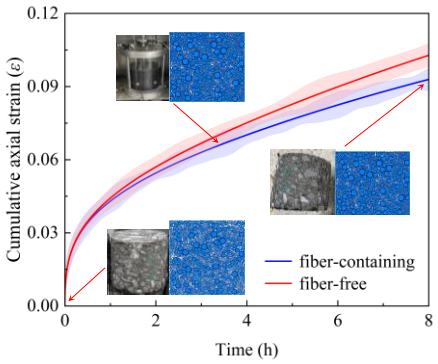
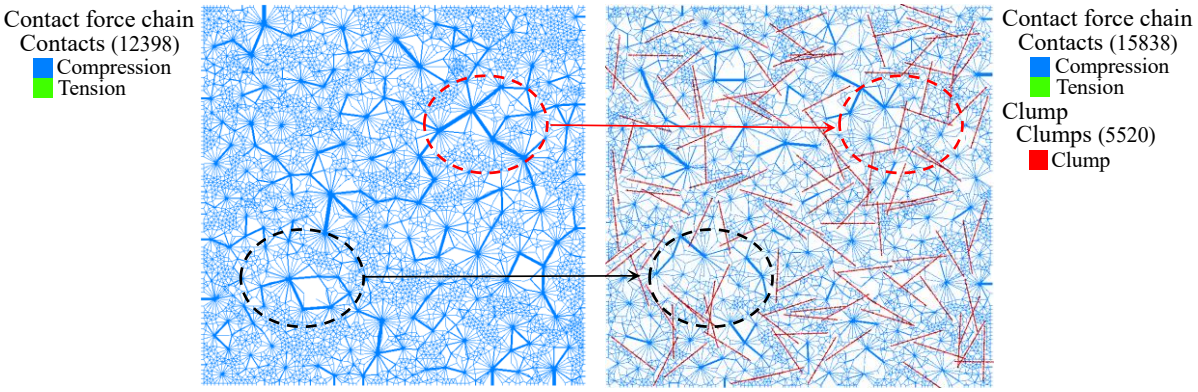


Figure 6. Average creep curves with shaded standard deviation (SD) bands for ordinary asphalt concrete and BFAC specimens (three replicate specimens per material group).

To examine whether this moderate macroscopic improvement is accompanied by mesoscopic load-path redistribution, Figure 7 compares the DEM contact-force networks of ordinary asphalt concrete and BFAC. In the plotting convention, blue denotes compressive contact-force chains and green denotes tensile chains, while the red clumps in the BFAC model represent the equivalent fiber bundles. Because distinct tensile chains are not sufficiently resolved at the present figure scale, the interpretation is restricted to the compressive load-transfer network, and no inference regarding tensile stresses is made from this figure. The subsequent analysis therefore focuses on the number, continuity, and spatial distribution of compressive force chains to assess whether BF provides additional load-transfer paths and promotes a more distributed load-bearing network. Together with the post-creep comparison in Figure 8, this analysis provides a contact-scale interpretation of the experimental trend rather than independent validation of the measured creep-rate reduction.

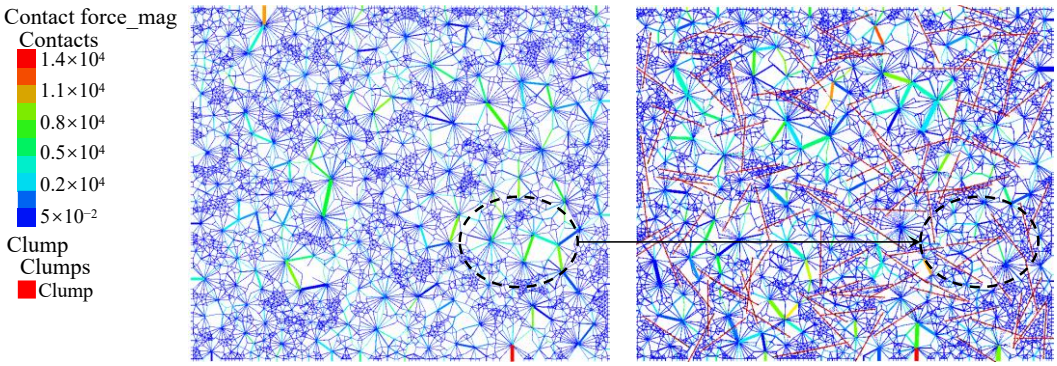


(**a**) Ordinary asphalt concrete. (**b**) BFAC (9 mm, 0.4%).

Figure 7. Contact-force chain distributions in ordinary asphalt concrete and BFAC (9 mm, 0.4%).

Figure 7a shows that the load-bearing network of ordinary asphalt concrete contained 12,398 contact-force chains. In Figure 7b, BF provided additional load-transfer paths and increased the corresponding count to 15,838, an increase of 27.75%. The BFAC plot also contained fewer visually dominant thick compressive chains, suggesting a more distributed contact-force network under the modeled condition. These contact counts are model-specific and are consistent with, but do not independently prove, the lower plotted creep rate shown in Figure 6.

Figure 8 compares the force chain distribution between ordinary asphalt concrete and BFAC specimens after creep loading.



(**a**) Ordinary asphalt concrete (**b**) BFAC (9 mm, 0.4%)

Figure 8. Contact-force chain distributions after creep deformation.

Comparison of Figure 8a,b indicates a more distributed contact-force network in BFAC under the modeled condition. For ordinary asphalt concrete, the maximum and minimum contact forces were 1.36×10^4 N and 6.22×10^{-2} N, respectively, compared with 1.30×10^4 N and 5.76×10^{-2} N for BFAC. These quantities are forces, not stresses. The smaller extreme contact forces suggest reduced local force concentration and more uniform load transfer, although the comparison is specific to the equivalent model conditions and loading stage used in the simulations.

5.2. Effect of Temperature on the Creep Characteristics of BFAC

To examine temperature-dependent creep, numerical simulations were conducted at −4, 0, 4, and 8 °C using the fixed experimental fiber configuration (9 mm, 0.4%). Figure 9 compares the simulated strain-time curves with the corresponding laboratory measurements. The 0 MPa tests at the four temperatures were used for parameter calibration, whereas the tests at 0.2, 0.4, and 0.6 MPa were reserved for model validation; the same confining pressure condition was not used for both purposes.

Figure 9 shows that the model reproduces the principal experimental trends, and the RMSE values provide quantitative measures of agreement for both calibration and validation conditions. Under each confining pressure, axial strain increased with time and was generally higher at higher temperatures for a common loading time. The strain at 8 °C was approximately 10–30% higher than that at −4 °C, with larger differences under low confinement. At 0.2 and 0.4 MPa, the strain difference between 8 and −4 °C after approximately 2 h was 0.02–0.03. These descriptive comparisons are specific to the investigated temperature and stress ranges.

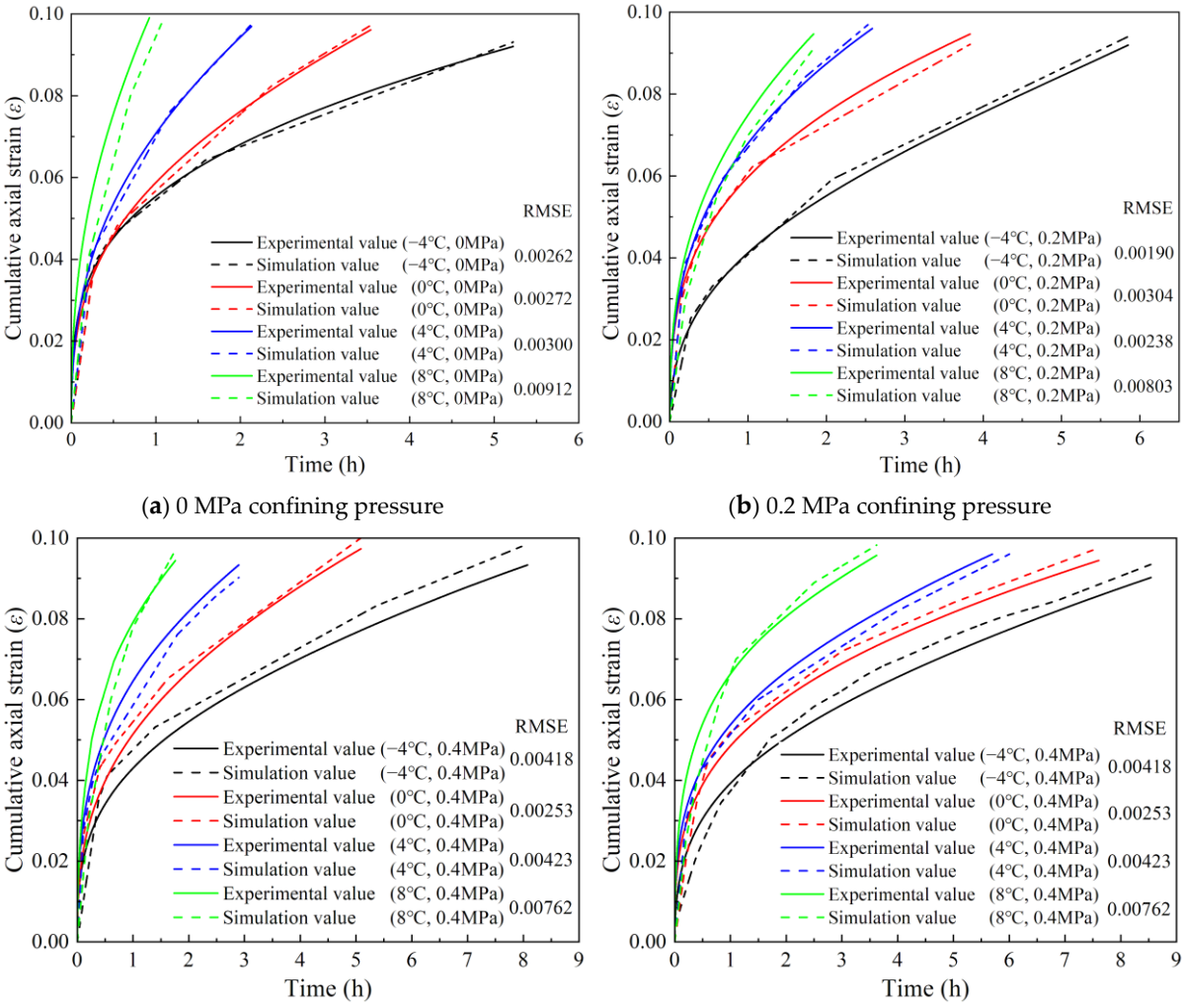


Figure 9. Experimental and simulated creep curves of BFAC at different temperatures and confining pressures.

For each temperature-confinement condition, the RMSE was calculated using the arithmetic-mean experimental curve and the corresponding simulated curve. Depending on the test duration, the mean experimental curves contained 1863–5580 sampled time points, whereas the simulated curves contained 3667–6152 output points. The experimental time coordinates were used as the reference for data pairing. When a simulated output was available at an identical time coordinate, the experimental and simulated strains were paired directly; otherwise, the simulated strain at that experimental time coordinate was obtained by linear interpolation between the two adjacent simulated output points. Owing to the dense sampling of both datasets, this interpolation was used only to align their time grids. The comparison was restricted to the common time interval covered by the two curves, ending at the last experimental time point; simulated output beyond that endpoint was excluded. The RMSE [45,46] was calculated using Equation (7).

$$\mathrm{RMSE}=\sqrt{\frac{1}{n}\sum_{i=1}^{n}\left[\varepsilon_{\mathrm{sim}}\left(t_i\right)-\varepsilon_{\mathrm{exp,mean}}\left(t_i\right)\right]^2} \tag{7}$$

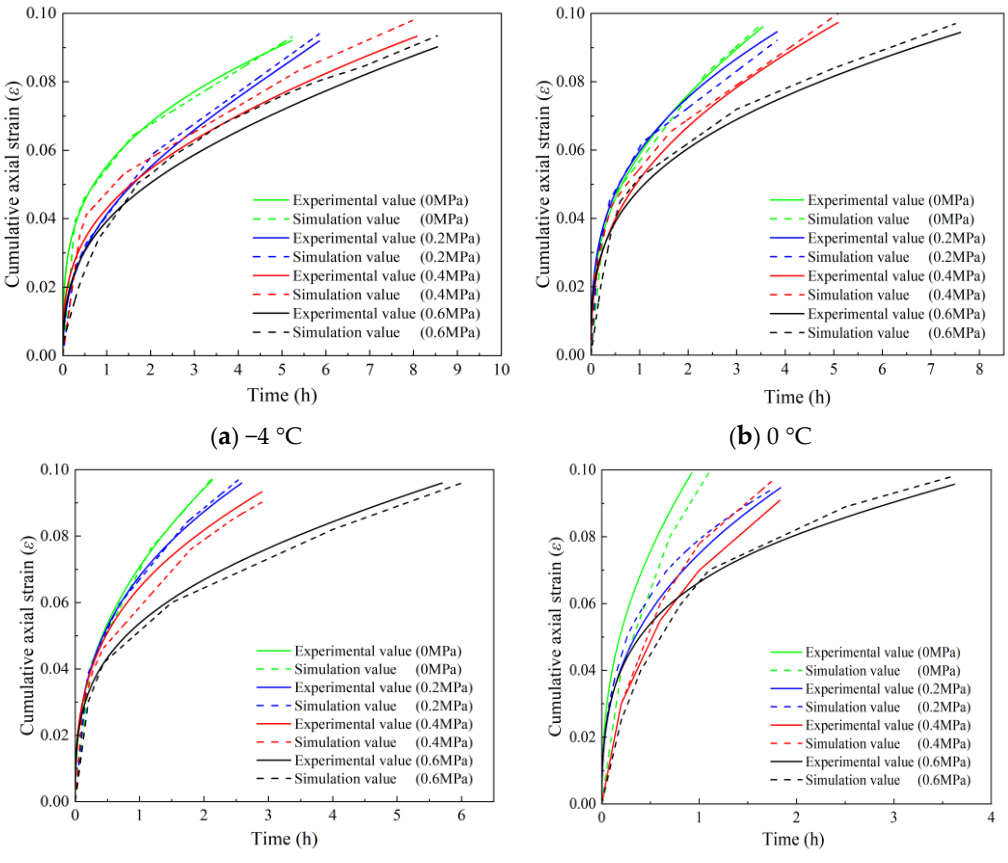
where t_i is an included experimental time coordinate, $\varepsilon_{\mathrm{exp,mean}}(t_i)$ and $\varepsilon_{\mathrm{sim}}(t_i)$ are the corresponding mean experimental and simulated axial strains, respectively, and n is the number of matched time points for that condition.

Across the 16 temperature-confinement conditions, the RMSE ranges from 0.00190 to 0.00912 in axial-strain units, with an average of 0.00421. At −4, 0, and 4 °C, the RMSE values range from 0.00190 to 0.00423, whereas those at 8 °C range from 0.00599 to 0.00912. The largest RMSE occurs at 8 °C and 0 MPa. These results indicate closer agreement at −4 to 4 °C and larger deviations at 8 °C, particularly under low confinement. Therefore, the model captures the principal experimental trends within the investigated conditions.

Further analysis of Figure 9d shows rapid strain growth during the first 0–1 h, followed by a gradual decrease in curve slope. At 3.5 h, the cumulative axial strains at −4, 0, 4, and 8 °C were 0.062, 0.075, 0.085, and 0.095, respectively, with increments of 0.013, 0.010, and 0.010 between adjacent temperatures. The early-stage slopes at 4 and 8 °C were higher than those at −4 and 0 °C, whereas the middle- and late-stage curves continued to rise at decreasing rates. This behavior is consistent with progressive contact-state adjustment and reduced particle rearrangement under sustained simulated loading.

5.3. Effect of Confining Pressure on the Creep Characteristics of BFAC

To examine confinement effects, numerical simulations were conducted at 0, 0.2, 0.4, and 0.6 MPa for the fixed experimental fiber configuration (9 mm, 0.4%). Figure 10 presents the resulting experimental and simulated strain-time curves. The simulations were intentionally continued beyond the 8 h laboratory limit so that all conditions could be compared at the common strain threshold $\varepsilon = 0.095$. Thus, the 9.0 h obtained at −4 °C and 0.6 MPa is numerical time, not the duration of a physical test. Values beyond 8 h are used only for relative comparison and require long-duration experimental validation before absolute predictions are made.



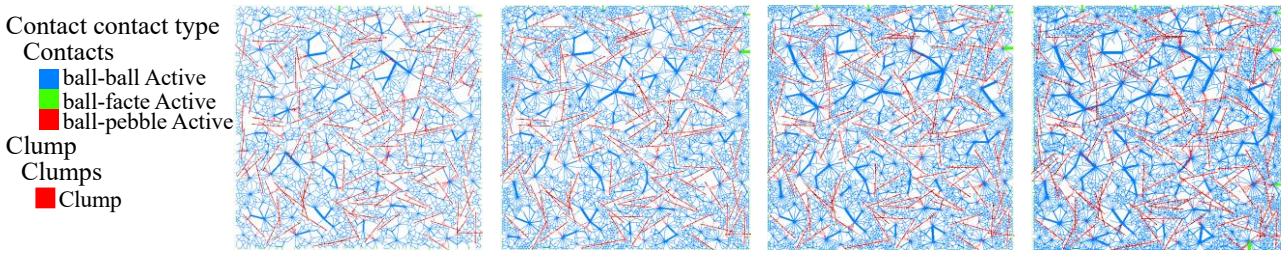
(**a**) −4 °C (**b**) 0 °C

(**c**) 4 °C (**d**) 8 °C

Figure 10. Experimental and simulated creep curves of BFAC under different confining pressures.

As shown by the simulated curves in Figure 10, higher confining pressure increased the time required to reach a given strain. At ε = 0.095, increasing confinement from 0 to 0.6 MPa extended the simulated time from 1.0 to 3.8 h at 8 °C, from 2.1 to 5.8 h at 4 °C, from 3.2 to 7.8 h at 0 °C, and from 5.0 to 9.0 h at −4 °C. At a common simulated time of 2 h, increasing confinement from 0 to 0.2, 0.4, and 0.6 MPa reduced strain at 4 °C from 0.095 to 0.090, 0.083, and 0.068, respectively (reductions of 5%, 13%, and 28%); the corresponding reductions were 5%, 12%, and 21% at 0 °C and 7%, 13%, and 20% at −4 °C. The results indicate stronger deformation constraint at 0.4–0.6 MPa than at 0.2 MPa, while values beyond the experimental duration remain numerical extrapolations.

Figure 11 presents the force chain distributions of BFAC specimens with the same fiber configuration at 8 °C and confining pressures of 0, 0.2, 0.4, and 0.6 MPa. As confining pressure increased, the compressive force chains became denser and more continuous and the contact network developed further. The corresponding contact counts increased from 7207 to 8420, 9410, and 12,110, respectively, indicating closer particle packing and reduced pore space in the two-dimensional model.



(**a**) 0 MPa (**b**) 0.2 MPa (**c**) 0.4 MPa (**d**) 0.6 MPa

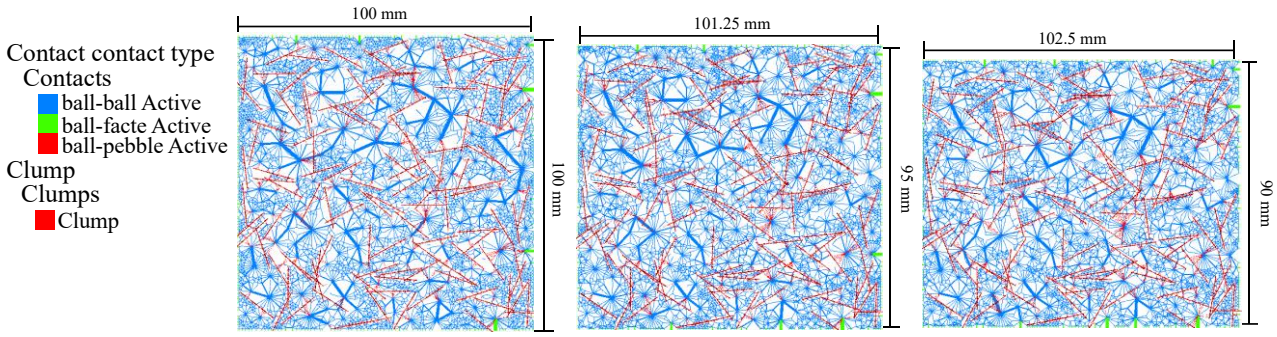
Figure 11. Force chain distributions of BFAC under varying confining pressures.

6. Discussion

6.1. Particle Motion Analysis During Creep

During BFAC creep, particle contacts and force states are continuously adjusted. To examine this process, the BFAC model with 9 mm fibers and 0.4% content was analyzed at 8 °C and 0.6 MPa confining pressure at three stages: unloading (axial strain = 0), intermediate loading (axial strain = 5%), and late loading (axial strain = 10%).

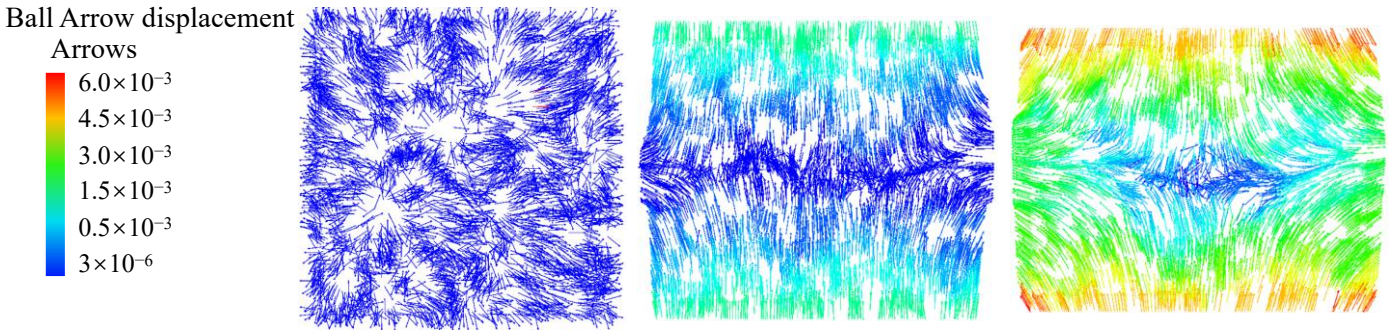
As illustrated in Figure 12, the number of internal contacts increased from 12,110 to 17,357 during loading, with a growth rate of 43.33%. This indicates that contact reconstruction occurred among particles throughout the loading process, leading to the propagation of compressive force chains and the formation of a new load-bearing network. When the axial strain further increased from 5% to 10%, the number of contact points slightly decreased from 17,357 to 17,302, revealing that the internal force chain network tended to stabilize at this stage. Thus, the subsequent macroscopic deformation is mainly attributed to local adjustment within the existing load-bearing structure rather than large-scale generation of new contacts.



(**a**) Unloaded stage (**b**) Mid-loading stage (**c**) Late-loading stage

Figure 12. Force chain distributions of the BFAC model at various stages (0.6 MPa, 8 °C).

Figure 13 presents particle displacement fields at 8 °C and 0.6 MPa confining pressures, with arrows indicating movement direction. Before loading, local displacement directions were scattered. At 5% axial strain, particle movement became more aligned with axial compression, and particles near the upper and lower boundaries moved toward the specimen center, forming a relatively stable central region. At 10% axial strain, displacement accumulation became more pronounced near the boundaries while the central region remained comparatively stable, indicating deformation dominated by compression and local slipping under the existing structural constraints.



(**a**) Unloaded stage (**b**) Mid-loading stage (**c**) Late-loading stage

Figure 13. Particle displacement fields of the BFAC model at various stages (0.6 MPa, 8 °C).

6.2. Effects of Fiber Length and Fiber Content

Previous studies have shown that BF length and content influence the mechanical performance of modified asphalt concrete [47,48]. The physical experiments in this study used only the 9 mm, 0.4% configuration. The effects of other fiber lengths (3 and 6 mm) and contents (0.2 and 0.3%) were examined exclusively through numerical simulations using the calibrated model; these results are predictions rather than additional experimental findings.

Figure 14 compares simulated creep curves for fiber lengths of 3, 6, and 9 mm at 0.3% content and for contents of 0.2%, 0.3%, and 0.4% at 9 mm length. The simulations were continued to approximately 15 h to compare curve development and the time required to reach common strain thresholds. This duration intentionally exceeds the 8 h laboratory limit. Because all curves approach approximately 0.10 axial strain at termination, relative performance is assessed using strain at common times and the time to reach $\varepsilon = 0.095$, rather than final cumulative strain. Absolute strains and times beyond the experiments remain unvalidated extrapolations.

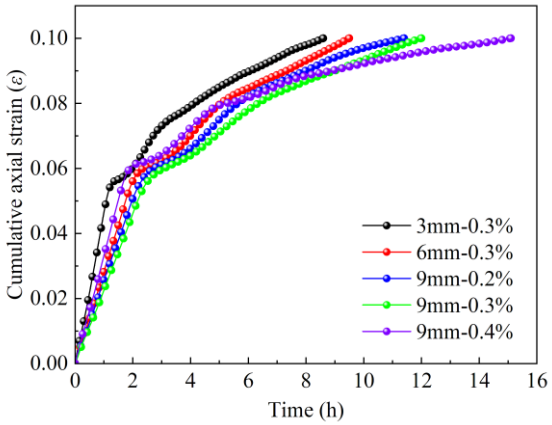
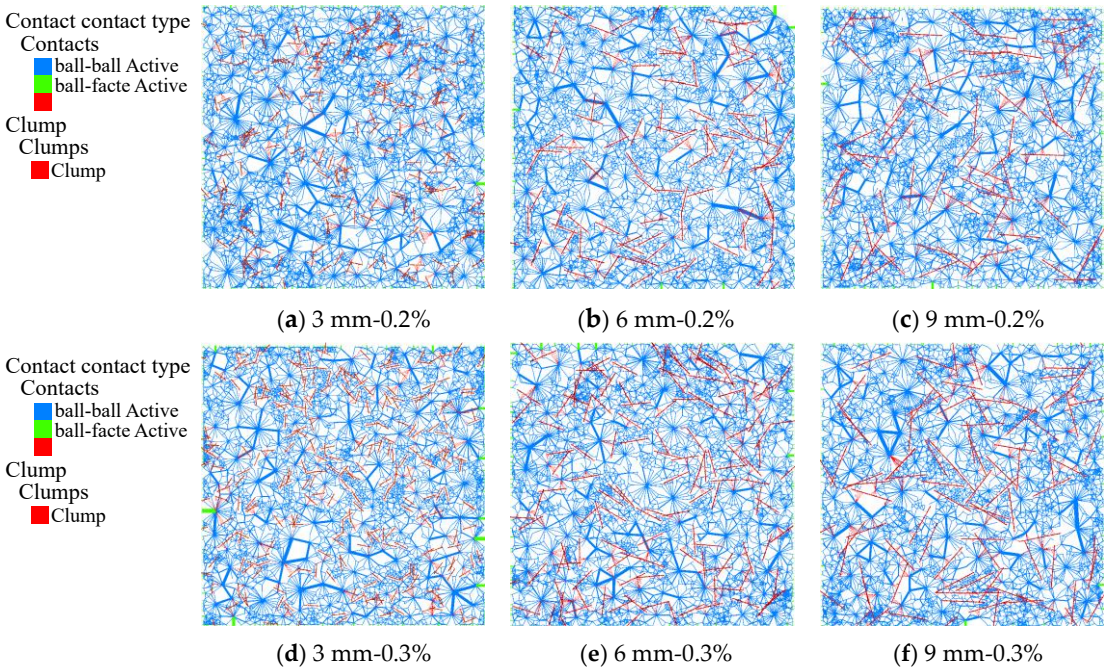


Figure 14. Simulated creep curves for different fiber lengths and contents. Relative comparisons use strain at common loading times and the time to reach $\varepsilon = 0.095$; the numerical time extends beyond the 8 h laboratory test limit.

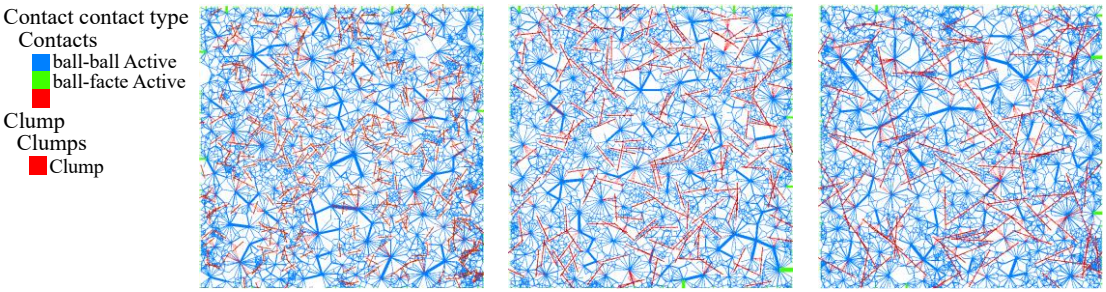
At a fixed content of 0.3%, the simulated time to reach ε = 0.095 increased in the order 3, 6, and 9 mm, indicating delayed threshold attainment with increasing fiber length. At a fixed length of 9 mm, the 0.4% configuration reached this threshold latest, followed by the 0.3% and 0.2% configurations. The curves cross, and the 0.4% configuration does not exhibit the lowest strain at every early or intermediate time; its relative advantage lies primarily in slower late-stage development and delayed threshold attainment. Thus, 9 mm and 0.4% is the most favorable configuration among those investigated numerically, not a universally optimal mixture and not the configuration with a uniquely smallest final cumulative strain.

Figure 15 shows the force chain and fiber distributions of simulated BFAC specimens with various fiber lengths and fiber contents. All force chain comparisons used equivalent discretization and identical temperature, confining pressure, and axial strain stage within each comparison series; only fiber length or fiber content was varied.



(**a**) 3 mm-0.2% (**b**) 6 mm-0.2% (**c**) 9 mm-0.2%

(**d**) 3 mm-0.3% (**e**) 6 mm-0.3% (**f**) 9 mm-0.3%



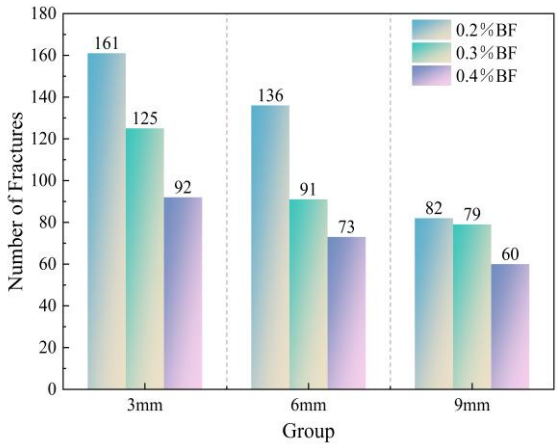
(**g**) 3 mm-0.4% (**h**) 6 mm-0.4% (**i**) 9 mm-0.4%

Figure 15. Force chain and fiber distributions under various fiber lengths and fiber contents.

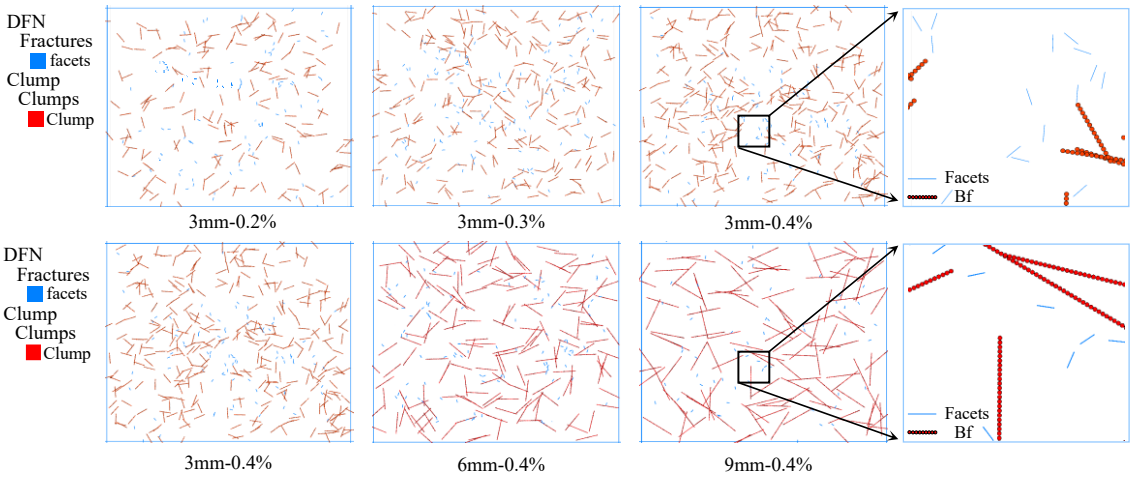
As shown in Figure 15a–i, for a fixed fiber length, the number of fiber-related contact points increased significantly, and the fibers became more densely distributed in the particle skeleton as the fiber content rose from 0.2% to 0.4%. At a fiber content of 0.2%, the fibers were sparsely distributed with discrete and localized contact with surrounding particles. When the fiber content increased to 0.3%, the fiber distribution became uniform with more connection nodes and continuous force chain transmission. When the fiber content further increased to 0.4%, the fiber contact network was further improved. This indicates that a higher fiber content is more conducive to maintaining the integrity and stability of the internal force chain structure of BFAC under long-term loading.

From Figure 15a–i, under a constant fiber content, the bridging effect of fibers on the particle skeleton gradually strengthened, and the stress transfer inside the specimen evolved from local and dispersed contacts to a continuous force chain structure as the fiber length increased from 3 mm to 9 mm. It can be seen that 3 mm fibers, due to their short length, were limited to connecting adjacent particles and only provided local constraints, failing to form long-distance force transfer paths; 6 mm fibers could connect more aggregate particles with stable bridging performance and improved force chain continuity; 9 mm fibers demonstrated cross-particle connection capacity to construct longer load transfer path, thereby enhancing the overall skeleton stability and mitigating structural rearrangement under sustained loading.

Parallel-bond cracking between asphalt mastic and aggregates/BF provides a model-based indicator of microcrack development during creep. Figure 16a reports the full factorial set of fiber lengths (3, 6, and 9 mm) and fiber contents (0.2%, 0.3%, and 0.4%). All microcrack comparisons used equivalent discretization and identical temperature, confining pressure, and axial-strain stage; only fiber length or fiber content was varied.



(**a**) Crack counts.



(**b**) Morphological distribution of cracks.

Figure 16. Simulated microcrack statistics and morphology for different BF lengths and contents.

Overall, as can be seen from Figure 16a, the number of internal microcracks in the specimen showed a downward trend with the increase in fiber length and fiber content. Under the same fiber content, when the fiber length increased from 3 mm to 9 mm, the number of microcracks decreased from 161 to 82, from 125 to 79, and from 92 to 60 for fiber contents of 0.2%, 0.3%, and 0.4%, respectively, indicating that increasing fiber length can suppress crack propagation inside the specimen.

In terms of fiber content variation, with the fiber content increasing from 0.2% to 0.4% under the same fiber length, the number of microcracks decreased from 161 to 92, from 136 to 73, and from 82 to 60 for fiber lengths of 3 mm, 6 mm, and 9 mm, with reductions of 42.86%, 46.32%, and 26.83%, respectively. This indicates that appropriately increasing fiber content is conducive to reducing the number of microcracks. Among the simulated configurations, the 9 mm, 0.4% specimen had the lowest reported crack count. This result supports a favorable relative trend within the investigated numerical range.

Figure 16b shows two compared series: the top row shows variations in fiber content from 0.2% to 0.4% at a fixed length of 3 mm, whereas the bottom row shows variations in fiber length from 3 to 9 mm at a fixed content of 0.4%. The 3 mm, 0.4% configuration therefore appears in both rows as the common reference. No crack paths were reported through the equivalent fiber bundles under the adopted model assumptions; this numerical observation is not experimental proof that fibers cannot fracture. Longer fibers reduced continuous crack path development in the simulations, consistent with the relative trend in crack counts.

6.3. Analysis of BFAC Creep Mechanism

The creep characteristics of BFAC are jointly governed by multiple factors, including fiber addition, temperature, confining pressure, and fiber length and fiber content. Based on the above results, the mesoscopic creep mechanism of BFAC under multi-factor action was summarized, as illustrated in Figure 17.

It can be seen from Figure 17a that the incorporation of BF altered the internal contact relationship and load transfer mode of BFAC. Without BF, the specimen mainly transferred load through local contacts between asphalt mastic and aggregates, manifesting short and scattered load transfer paths. After adding BF, the fibers formed a bridging effect between particle skeletons, which increased effective connections between particles and improved the internal load transfer structure, allowing loads to be transferred along

more continuous paths. This ultimately enhanced the overall stability of the skeleton while reducing creep deformation.

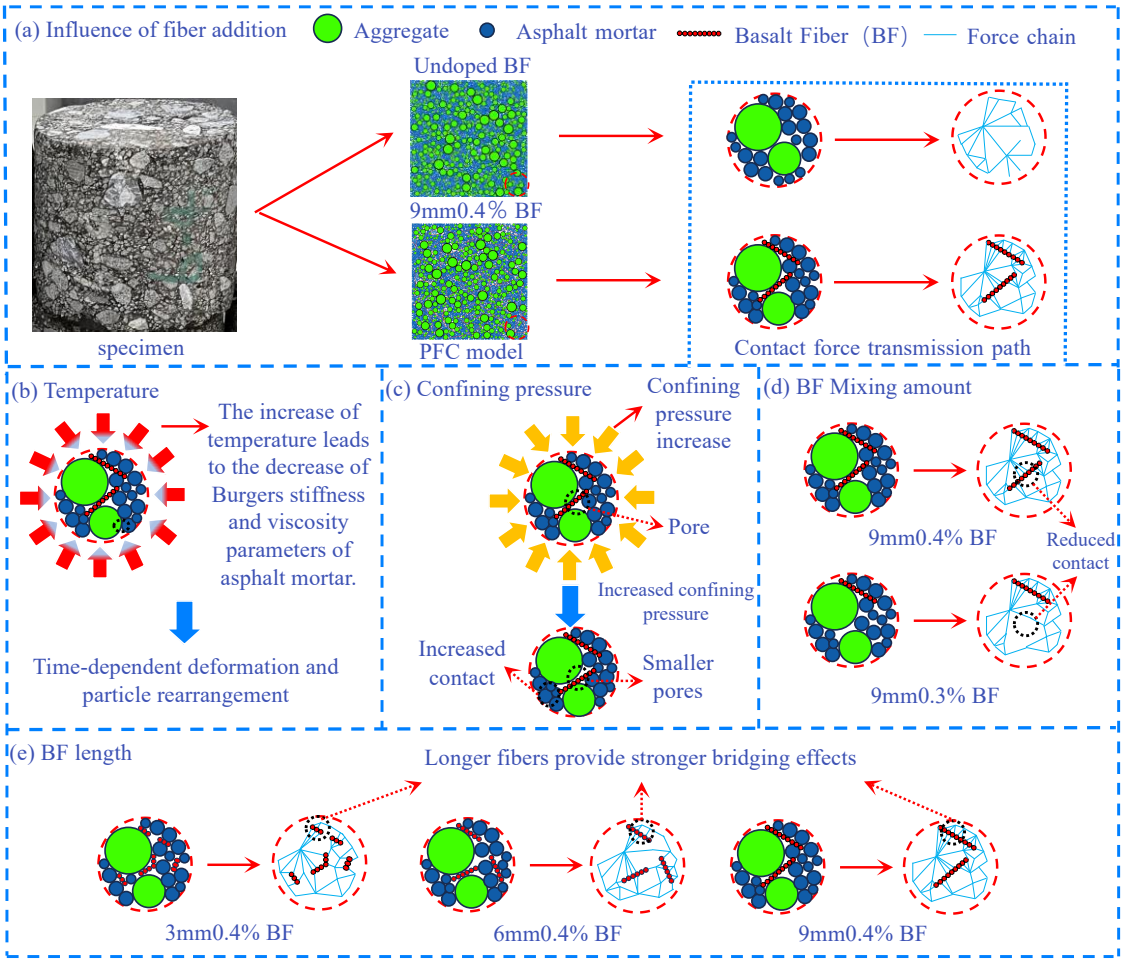


Figure 17. Mesoscopic creep mechanism of BFAC under multi-factor action.

Figure 17b illustrates the modeled effect of temperature on BFAC creep. In the constitutive implementation, increasing temperature reduces the Burgers stiffness and viscosity parameters of asphalt mastic, making time-dependent deformation and particle rearrangement more likely. The parallel-bond parameters of mastic-aggregate and mastic-fiber interfaces remain fixed; therefore, the simulations demonstrate mastic viscoelastic softening rather than temperature-induced degradation of interface bond strength.

Figure 17c shows that confining pressure suppresses the creep development of BFAC mainly by enhancing the compaction effect of the particle skeleton. With increasing confining pressure, internal pores of the specimen were compressed, resulting in a closer particle arrangement and more particle contacts, which improved the load-bearing capacity and stability of the skeleton structure. This indicates that increasing confining pressure is conducive to strengthening inter-particle constraints and restricting particle rearrangement and sliding.

Figure 17d shows that, for a fixed fiber length, increasing fiber content increased fiber-particle contacts and produced a denser planar load-transfer network in the simulations. Within the investigated range, the 0.4% content was the most favorable numerical configuration for restraining late-stage creep and reducing crack counts. This finding is limited to the modeled contents and does not exclude agglomeration or reduced workability at higher contents.

Figure 17e reveals that, under the same fiber content, increasing fiber length enhanced the bridging capacity of fibers to the particle skeleton. Specifically, short fibers mainly acted between adjacent particles, mostly providing local constraints. With increasing fiber length, the cross-particle connection capacity of BFAC was continuously enhanced, forming longer load transfer paths and making the skeleton structure more stable. In contrast, 9 mm fibers exhibited stronger bridging and stabilizing effects, which are more favorable for improving the creep resistance of BFAC.

The results identify distinct roles for temperature, confining pressure, and BF in the experimental and numerical responses. Higher temperature increased creep strain through the prescribed viscoelastic softening of asphalt mastic, whereas increased confining pressure delayed attainment of a common strain and increased modeled particle contacts. BF addition provided additional load-transfer paths and reduced the plotted creep rate under the tested condition. Longer fibers and higher contents delayed threshold attainment and reduced simulated crack counts within the investigated numerical range, consistent with the general reinforcement trends reported by Xing et al. [49], Guo et al. [50], Yang et al. [51], and Feng et al. [52]. These agreements concern directional trends rather than exact quantitative validation across different materials and test protocols. The present evidence supports contact-level interpretation of comparative creep behavior, but does not justify direct prediction of deformation over the service life of hydraulic structures.

6.4. Experimental Variability, Numerical Uncertainty, and Scope

Three replicate specimens were tested per material group and condition, and the plotted laboratory curves are arithmetic means. In Figure 6, the shaded bands represent the standard deviation (SD) of the three replicate specimens at each time point, thereby indicating specimen-level variability. In Figure 9, error bands are omitted to preserve clarity in the direct comparison between the mean experimental curves and the simulated curves across the 16 temperature-confinement conditions; the corresponding RMSE values are used to quantify their agreement. Therefore, the 9.58% reduction in creep rate is interpreted as a descriptive difference between the mean curves, not as evidence of statistical significance. Additional replication and statistical analysis are required before generalizing the magnitude of the fiber effect.

Numerical results are subject to uncertainty from particle generation, fiber placement and orientation, discretization, and calibrated parameters. No repeated-realization or systematic sensitivity results are reported; consequently, the associated variability cannot be quantified from this study. Only comparative simulations under equivalent model settings are interpreted, and absolute contact counts, crack counts, and displacement magnitudes remain model-specific.

The two-dimensional idealization, fixed interfacial parallel-bond parameters, and extrapolation beyond the 8 h laboratory tests further limit quantitative prediction. Long-duration experiments, three-dimensional simulations, temperature-dependent interface calibration, and uncertainty analyses are needed before the results can be used for service-life prediction in hydraulic anti-seepage structures.

7. Conclusions

We conducted a feasibility study of the temperature-corrected Burgers model for characterizing the creep characteristics of BFAC by combining creep tests and discrete element simulations. Furthermore, the reinforcing mechanism of BF, the effects of temperature and confining pressure on BFAC creep characteristics, and the influences of fiber length and fiber content were investigated. The main conclusions are as follows:

(1) Temperature and confining pressure significantly affected BFAC creep under the investigated conditions. Higher temperature increased creep deformation through viscoelastic softening of asphalt mastic; it did not prescribe a reduction in mastic-aggregate or mastic-fiber bond strength because those parallel-bond parameters were fixed. Higher confining pressure increased particle contacts and structural constraint and delayed attainment of a common strain threshold.

(2) In the early stage of creep loading, BFAC is mainly characterized by particle position adjustment and contact reconstruction. After the middle and late stages of loading, the particle contact relationship tends to be stable, and the internal force transmission structure is basically formed. The macroscopic deformation mainly comes from the particle slip and local adjustment under the existing skeleton constraints. Longer BF is beneficial for enhancing the long-scale connection ability between particles, and higher BF content produced a denser planar force-transfer network in the two-dimensional simulations, thus improving the overall structural stability of the material.

(3) Among the fiber configurations examined numerically, 9 mm fibers at 0.4% content were the most favorable in terms of delayed attainment of the common strain threshold and reduced simulated crack counts. This is not a universal optimum: only this configuration was tested physically, the other configurations were numerical predictions, and no statistical superiority was established. The findings provide a comparative reference for mixture development, while long-term applications in hydraulic structures require longer experiments, three-dimensional simulations, and uncertainty assessment to achieve.

Author Contributions: K.W.: Conceptualization, Resources, Writing—review & editing. S.X.: Supervision, Formal analysis, Validation. R.H.: Methodology, Software, Writing—original draft. D.F.: Formal analysis, Validation. Y.W.: Data curation, Formal analysis. Y.L.: Funding acquisition, Formal analysis. All authors have read and agreed to the published version of the manuscript.

Funding: This research was funded by National Natural Science Foundation of China (Grant no. 52379127) and Qinghai Institute of Technology for the support of 'Kunlun Talent' Talent Introduction Research Project (2025-QLGKLYCZX-034).

Data Availability Statement: The data that support the findings of this study are available from the corresponding author upon reasonable request.

Acknowledgments: The authors appreciate the financial support from the National Natural Science Foundation of China (Grant no. 52379127) and Qinghai Institute of Technology for the support of "Kunlun Talent" Talent Introduction Research Project (2025-QLGKLYCZX-034). The views and findings of this study represent those of the authors and may not reflect those of the financial support agencies.

Conflicts of Interest: The authors declare that they have no known competing financial interests or personal relationships that could have appeared to influence the work reported in this paper.

References

1. Han, M.; Chen, K.; Feng, Y.; Zou, D.; Huang, Q. Cross-scale refined analysis and reinforcement design for the rigid-flexible mixed region in hybrid dams. *Comput. Geotech.* **2024**, *176*, 106727. https://doi.org/10.1016/j.compgeo.2024.106727.
2. Li, G.; Zhu, Q.; Liu, J.; Liu, C.; Zhang, J. Study on the shear strength and erosion resistance of sand solidified by enzyme-induced calcium carbonate precipitation (EICP). *Materials* **2024**, *17*, 3642. https://doi.org/10.3390/ma17153642.
3. Kilit, M.; Cavus, U.S.; Zorluer, I. Leakage problem and safety assessment of an embankment dam: Investigations and solution. *J. Perform. Constr. Facil.* **2023**, *37*, 04023046. https://doi.org/10.1061/JPCFEV.CFENG-4257.
4. Li, C.; Song, Z.; Wang, F.; Wang, Z.; Liu, Y. Seismic analysis of asphalt concrete core rockfill dams considering the bimodulus effect. *Soil Dyn. Earthq. Eng.* **2024**, *187*, 108984. https://doi.org/10.1016/j.soildyn.2024.108984.

5. Peng, H.; Qian, N.; Yin, D.; Luo, W. Modeling interface damage with random interface strength on asphalt concrete impervious facings. *Materials* **2024**, *17*, 3310. https://doi.org/10.3390/ma17133310.
6. Bao, L.; He, M.; Wang, S.; Wu, X. Study on the effect of asphalt static conditions on the tensile properties of acidic aggregate hydraulic asphalt concrete. *Materials* **2024**, *17*, 2627. https://doi.org/10.3390/ma17112627.
7. Gao, J.; Han, W.; Dang, F.; Xue, H.; Ren, J. Analytical force and deformation analysis model of an asphalt concrete core based on the Winkler elastic foundation plate theory. *Int. J. Geomech.* **2026**, *26*, 04026071. https://doi.org/10.1061/IJGNAI.GMENG-11930.
8. Phung, B.N.; Le, T.-H.; Mai, H.T.; Nguyen, T.-A.; Ly, H.-B. Advancing basalt fiber asphalt concrete design: A novel approach using gradient boosting and metaheuristic algorithms. Case Stud. *Constr. Mater.* **2023**, *19*, e02528. https://doi.org/10.1016/j.cscm.2023.e02528.
9. Ji, X.; Yuan, Y.; Huang, Y.; Shao, J.; Li, S. Performance study of asphalt mixtures reinforced with gradated basalt fibers of mixed lengths. *Materials* **2024**, *17*, 4706. https://doi.org/10.3390/ma17194706.
10. Long, A.; Sun, X.; Yu, Z.; Zhang, B.; Zhang, G.; Huang, P.; Wang, J. Experimental study and mechanism analysis on the basic mechanical properties of hydraulic basalt fiber asphalt concrete. *Mater. Struct.* **2022**, *55*, 161. https://doi.org/10.1617/s11527-022-02001-y.
11. Zhang, C.; Shi, F.; Cao, P.; Liu, K. The fracture toughness analysis on the basalt fiber reinforced asphalt concrete with prenotched three-point bending beam test. *Case Stud. Constr. Mater.* **2022**, *16*, e01079. https://doi.org/10.1016/j.cscm.2022.e01079.
12. Gui, W.; Hu, X.; Wang, L.; Li, C.; Zhang, F.; Tian, Z.; Cao, J. Multi-scale fracture performance and mechanisms of basalt fiber reinforced warm recycled asphalt mixtures under freeze-thaw cycles and various fracture modes. *Theor. Appl. Fract. Mech.* **2026**, *143*, 105520. https://doi.org/10.1016/j.tafmec.2026.105520.
13. Hassanjani, M.H.; Arabani, M.; Nejad, F.M.; Shalchian, M.M. Evaluation of the impacts of basalt fibers and hydrothermal liquefaction bio-oil on the fracture properties of asphalt mixtures at intermediate and low temperatures. *Results Eng.* **2026**, *29*, 109075. https://doi.org/10.1016/j.rineng.2026.109075.
14. Long, A.; Sun, X.; Zhang, G.; Yu, Z.; Zhang, B.; Huang, P.; Wang, J.; Wen, L. Study on fracture performance and failure mechanism of hydraulic basalt fiber asphalt concrete by considering temperature effect. *Theor. Appl. Fract. Mech.* **2023**, *125*, 103895. https://doi.org/10.1016/j.tafmec.2023.103895.
15. Zhang, J.; Zhou, M.; Liu, J.; Huang, X. Experimental study of stress and deformation of reclaimed asphalt concrete at different temperatures. *Materials* **2023**, *16*, 1323. https://doi.org/10.3390/ma16031323.
16. Guo, Q.; Wang, H.; Gao, Y.; Jiao, Y.; Liu, F.; Dong, Z. Investigation of the low-temperature properties and cracking resistance of fiber-reinforced asphalt concrete using the DIC technique. *Eng. Fract. Mech.* **2020**, *229*, 106951. https://doi.org/10.1016/j.engfracmech.2020.106951.
17. Zhang, X.; Liu, J. Viscoelastic creep properties and mesostructure modeling of basalt fiber-reinforced asphalt concrete. *Constr. Build. Mater.* **2020**, *259*, 119680. https://doi.org/10.1016/j.conbuildmat.2020.119680.
18. Dai, Q.; You, Z. Prediction of creep stiffness of asphalt mixture with micromechanical finite-element and discrete-element models. *J. Eng. Mech.* **2007**, *133*, 163–173. https://doi.org/10.1061/(ASCE)0733-9399(2007)133:2(163).
19. Liu, G.; Han, D.; Jia, Y.; Zhao, Y. Asphalt mixture skeleton main force chains composition criteria and characteristics evaluation based on discrete element methods. *Constr. Build. Mater.* **2022**, *323*, 126313. https://doi.org/10.1016/j.conbuildmat.2022.126313.
20. Xia, C.; Liu, Z.; Zhou, C. Burger's bonded model for distinct element simulation of the multi-factor full creep process of soft rock. *J. Mar. Sci. Eng.* **2021**, *9*, 945. https://doi.org/10.3390/jmse9090945.
21. Guo, W.; Wei, Y. Discrete element modeling on nanoindentation creep behavior of C-S-H under Berkovich and flat-tip indenters. *Cem. Concr. Res.* **2025**, *190*, 107808. https://doi.org/10.1016/j.cemconres.2025.107808.
22. Wang, H.; Wu, H.; Xiang, J.; Ye, G. Simulation of creep damage of asphalt mixture based on discrete element method. *J. Mater. Civ. Eng.* **2023**, *35*, 04023185. https://doi.org/10.1061/JMCEE7.MTENG-15074.
23. Wang, H.; Huang, W.; Cheng, J.; Ye, G. Mesoscopic creep mechanism of asphalt mixture based on discrete element method. *Constr. Build. Mater.* **2021**, *272*, 121932. https://doi.org/10.1016/j.conbuildmat.2020.121932.
24. Zhang, X.; Chen, E.; Li, N.; Wang, L.; Si, C.; Wang, C. Micromechanical analysis of the rutting evolution of asphalt pavement under temperature-stress coupling based on the discrete element method. *Constr. Build. Mater.* **2022**, *325*, 126800. https://doi.org/10.1016/j.conbuildmat.2022.126800.
25. Ma, T.; Zhang, D.; Zhang, Y.; Zhao, Y.; Huang, X. Effect of air voids on the high-temperature creep behavior of asphalt mixture based on three-dimensional discrete element modeling. *Mater. Des.* **2016**, *89*, 304–313. https://doi.org/10.1016/j.matdes.2015.10.005.
26. *DL/T 5362-2018*; Test Code for Hydraulic Asphalt Concrete. Electric Power Industry Standard of the People's Republic of China: Beijing, China, 2018.

27. Hui, Y.; Men, G.; Xiao, P.; Tang, Q.; Han, F.; Kang, A.; Wu, Z. Recent advances in basalt fiber reinforced asphalt mixture for pavement applications. *Materials* **2022**, *15*, 6826. https://doi.org/10.3390/ma15196826.
28. Qi, X.; Tian, S.; Shan, L.; Liu, S.; Wang, Y. Creep damage evolution process of asphalt binder based on viscoelastic characteristics. *J. Traffic Transp. Eng. (Engl. Ed.)* **2024**, *11*, 497–506. https://doi.org/10.1016/j.jtte.2022.07.006.
29. Zhou, F.; Scullion, T. Discussion: Three stages of permanent deformation curve and rutting model. *Int. J. Pavement Eng.* **2002**, *3*, 251–260. https://doi.org/10.1080/1029843021000083676.
30. Zhang, Q.; Gu, X.; Yu, Z.; Liang, J.; Dong, Q. Viscoelastic damage characteristics of asphalt mixtures using fractional rheology. *Materials* **2021**, *14*, 5892. https://doi.org/10.3390/ma14195892.
31. Zhang, Y.; Zhu, Y.; Wang, W.; Ning, Z.; Feng, S.; Höeg, K. Compressive and tensile stress-strain-strength behavior of asphalt concrete at different temperatures and strain rates. *Constr. Build. Mater.* **2021**, *311*, 125362. https://doi.org/10.1016/j.conbuildmat.2021.125362.
32. Wen, S.; Chen, J.; Lv, Y.; Shen, T.; Zhang, X. Experimental and modeling study on creep behavior of GFRP pipes dependent on temperature and stress. *Mater. Test.* **2026**, *68*, 1–13. https://doi.org/10.1515/mt-2025-0284.
33. Tarifard, A.; Török, Á.; Görög, P. Review of the creep constitutive models for rocks and the application of creep analysis in geomechanics. *Rock Mech. Rock Eng.* **2024**, *57*, 7727–7757. https://doi.org/10.1007/s00603-024-03939-x.
34. Huang, C.; Zhu, C.; Ma, Y.; Aluthgun Hewage, S. Investigating mechanical behaviors of rocks under freeze-thaw cycles using discrete element method. *Rock Mech. Rock Eng.* **2022**, *55*, 7517–7534. https://doi.org/10.1007/s00603-022-03027-y.
35. Zhang, J.; Chen, Y.; Du, R.; Zhao, X.; Wu, J. Macroscopic and microscopic mechanical characteristics and crack propagation behavior of sandstone-like samples with single cracks under freeze-thaw cycles: Experimental and numerical simulation. *Theor. Appl. Fract. Mech.* **2024**, *129*, 104201. https://doi.org/10.1016/j.tafmec.2023.104201.
36. Lesueur, D.; Elwardany, M.D.; Planche, J.-P.; Christensen, D.; King, G.N. Impact of the asphalt binder rheological behavior on the value of the ΔTc parameter. *Constr. Build. Mater.* **2021**, *293*, 123464. https://doi.org/10.1016/j.conbuildmat.2021.123464.
37. Liu, Y.; You, Z. Visualization and simulation of asphalt concrete with randomly generated three-dimensional models. *J. Comput. Civ. Eng.* **2009**, *23*, 340–347. https://doi.org/10.1061/(ASCE)0887-3801(2009)23:6(340).
38. Chen, X.; Peng, D.; Morrissey, J.P.; Ooi, J.Y. A comparative assessment and unification of bond models in DEM simulations. *Granul. Matter* **2022**, *24*, 29. https://doi.org/10.1007/s10035-021-01187-2.
39. Li, H.; McDowell, G.R. Discrete element modelling of under sleeper pads using a box test. *Granul. Matter* **2018**, *20*, 26. https://doi.org/10.1007/s10035-018-0795-0.
40. Xue, B.; Que, Y.; Pei, J.; Ma, X.; Wang, D.; Yuan, Y.; Zhang, H. A state-of-the-art review of discrete element method for asphalt mixtures: Model generation methods, contact constitutive models and application directions. *Constr. Build. Mater.* **2024**, *414*, 134842. https://doi.org/10.1016/j.conbuildmat.2023.134842.
41. Zhang, Z.H.; Zhang, G.D.; Li, M.D.; Liao, W.; Xu, Z.H. Influence analysis of meso-parameters on macro-mechanical properties of coarse-grained soil in particle flow code model. *J. Hydraul. Eng.* **2014**, *45*, 215–220. https://doi.org/10.13243/j.cnki.slxb.2014.s2.034.
42. Tan, F.; Yin, G.; Zhao, P.; Sun, G.; Li, Z.; Zhang, Z. DEM study on the effect of fiber length and content on the macro-micro mechanical behavior of fiber-sand mixture. *Sci. Rep.* **2026**, *16*, 4063. https://doi.org/10.1038/s41598-025-34063-7.
43. Cundall, P.A. A discontinuous future for numerical modelling in geomechanics? Proc. *Inst. Civ. Eng.-Geotech. Eng.* **2001**, *149*, 41–47. https://doi.org/10.1680/geng.2001.149.1.41.
44. Potyondy, D.; Cundall, P. A bonded-particle model for rock. *Int. J. Rock Mech. Min. Sci.* **2004**, *41*, 1329–1364. https://doi.org/10.1016/j.ijrmms.2004.09.011.
45. Willmott, C.J.; Matsuura, K. Advantages of the mean absolute error (MAE) over the root mean square error (RMSE) in assessing average model performance. *Clim. Res.* **2005**, *30*, 79–82. https://doi.org/10.3354/cr030079.
46. Hodson, T.O. Root-mean-square error (RMSE) or mean absolute error (MAE): When to use them or not. *Geosci. Model Dev.* **2022**, *15*, 5481–5487. https://doi.org/10.5194/gmd-15-5481-2022.
47. Zhao, H.; Guan, B.; Xiong, R.; Zhang, A. Investigation of the performance of basalt fiber reinforced asphalt mixture. *Appl. Sci.* **2020**, *10*, 1561. https://doi.org/10.3390/app10051561.
48. Lou, K.; Xiao, P.; Wu, B.; Kang, A.; Wu, X.; Shen, Q. Effects of fiber length and content on the performance of ultra-thin wearing course modified by basalt fibers. *Constr. Build. Mater.* **2021**, *313*, 125439. https://doi.org/10.1016/j.conbuildmat.2021.125439.
49. Xing, X.; Rao, X.; Zou, Y.; Li, H.; Zhang, L. Creep behavior of asphalt concrete core materials in embankment dams under a stepped loading path. *J. Mater. Civ. Eng.* **2021**, *33*, 04021233. https://doi.org/10.1061/(ASCE)MT.1943-5533.0003841.

50. Guo, Q.; Chen, Z.; Liu, P.; Li, Y.; Hu, J.; Gao, Y.; Li, X. Influence of basalt fiber on mode I and II fracture properties of asphalt mixture at medium and low temperatures. *Theor. Appl. Fract. Mech.* **2021**, *112*, 102884. https://doi.org/10.1016/j.tafmec.2020.102884.
51. Yang, Z.; Yang, W.; Yang, H.; Liu, L.; He, J. Study of stress-strain relationship of hydraulic asphalt concrete at low to intermediate temperatures based on experimental data regression. *Constr. Build. Mater.* **2023**, *409*, 134059. https://doi.org/10.1016/j.conbuildmat.2023.134059.
52. Feng, S.; Wang, W.; Hu, K.; Höeg, K. Stress-strain-strength behavior of asphalt core in embankment dams during construction. *Constr. Build. Mater.* **2020**, *259*, 119706. https://doi.org/10.1016/j.conbuildmat.2020.119706.

Disclaimer/Publisher's Note: The statements, opinions and data contained in all publications are solely those of the individual author(s) and contributor(s) and not of MDPI and/or the editor(s). MDPI and/or the editor(s) disclaim responsibility for any injury to people or property resulting from any ideas, methods, instructions or products referred to in the content.